

Kerr Electro-Optic Measurements and Nonuniform Electric Field Reconstructions

by

Tza-Jing Gung

B.S. Electrical Engineering, National Taiwan University (1992)

M.S. Electrical Engineering, Massachusetts Institute of Technology (1995)

Submitted to the Department of Electrical Engineering and Computer Science
in Partial Fulfillment of the Requirements for the Degree of
Doctor of Philosophy in Electrical Engineering

at the

Massachusetts Institute of Technology

May 1999

June 2000

© 1999 Massachusetts Institute of Technology

All rights reserved

Signature of Author

Department of Electrical Engineering and Computer Science

May 11, 1999

Certified by

Markus Zahn

Professor of Electrical Engineering

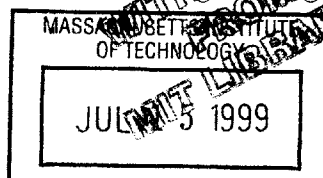
Thesis Supervisor

Accepted by

Arthur C. Smith

Chairman, Committee on Graduate Students

Department of Electrical Engineering and Computer Science



ENG

To my parents and brother

KERR ELECTRO-OPTIC MEASUREMENTS AND NONUNIFORM ELECTRIC FIELD RECONSTRUCTIONS

by

TZA-JING GUNG

Submitted to the Department of Electrical Engineering and Computer Science
on May 15, 1999 in Partial Fulfillment of the Requirements
for the Degree of Doctor of Philosophy in
Electrical Engineering

Abstract

This thesis uses Kerr electro-optical tomography as a new method to measure electric field and space charge distributions in insulating liquids when the applied electric field magnitude and direction are not constant along the light path. This technology can be used to experimentally verify the electrical design of high voltage devices, to monitor and diagnose the electrical health of high voltage devices and systems, to provide information on the remaining life, and to prevent failure caused by dielectric breakdown.

The Kerr electro-optic method passes low power laser light through a high voltage region filled with an insulating liquid, such as transformer oil. Because the insulating liquid becomes slightly birefringent under high electric field stress, incident linearly or circularly polarized light propagating through the high field stressed medium becomes elliptically polarized. By using a polariscope to analyze the elliptically polarized light due to electric field induced birefringence (Kerr effect), we can measure the electric field distribution in the insulating liquid so that the space charge distribution can be calculated from Gauss' law, $\rho = \nabla \cdot \epsilon \vec{E}$. Making use of the measured data, together with insulating liquid properties, such as dielectric constant, breakdown field strength, resistivity, dissipation factor, thermal conductivity, thermal stability limit, etc., optical measurements can help evaluate the electrical design and health of high voltage systems.

Because the Kerr effect in most liquids is very weak, the detected optical signal is very sensitive to electrical noise and small disturbances. In this thesis we studied methods to increase the optical signal level and to suppress electrical noise so that the measurement results can accurately recover the electric field using the "onion peeling"

method of radial discretization in axisymmetric geometries. Measurements were performed using low Kerr constant transformer oil ($B \approx 2.3 \times 10^{-15} \text{m/V}^2$) and high Kerr constant propylene carbonate ($B \approx 1 \times 10^{-12} \text{m/V}^2$) with parallel-plate, point-plane, and point-ring-plane electrode geometries. We also examine some measurements with non-axisymmetric electrode geometry. We compare experimentally determined electric field distributions with theoretical or computer simulated results under space charge free conditions to provide a comparison for nonzero space charge distributions. Theoretical analyses of significant space charge effects are presented for parallel-plate and coaxial cylindrical electrodes.

Thesis Supervisor: Markus Zahn

Title: Professor of Electrical Engineering

Acknowledgments

I wish to thank Prof. Markus Zahn, supervisor of my thesis, for helping and guiding me throughout my thesis research. It was my pleasure to work under his guidance during my four years at MIT. His enthusiasm for research helped me continue to make progress no matter what kind of problems I encountered.

I would like to express my gratitude to our technician Wayne Ryan who helped me design my experimental setup and shared his experience with me, and to Rocky Albano for his expertise in machining the high voltage electrode assemblies.

I am very fortunate to have the opportunity to work with the other Ph.D. students in the High Voltage Research Laboratory. They are Darrell Schlicker, Afsin Ustundag, Yanqing Du, and Alexander Mamishev. I especially thank Afsin for being my research partner in developing the Kerr electro-optic tomography technology.

I also want to thank Ansoft Corp. for providing their computer software Maxwell which was used for many of the computer simulations performed in this thesis, and to thank the MIT Department of Electrical Engineering and Computer Science for awarding me the Winton Hayes, Edwin S. Webster and Grass Instrument Co. Fellowship.

In addition, I also want to acknowledge the support by the National Science Foundation under Grant No. ECS922038 which funded the early part of this research program.

Finally, special warm appreciation is expressed to Wendy Wan-Chun Wang. Her support and encouragement helped me to finish this thesis.

Contents

Abstract	5
Acknowledgments	7
Contents	9
List of Figures	16
1 Introduction	29
1.1 Dielectric Liquids	29
1.2 Scope of Thesis	30
1.3 Outline of Thesis	31
2 Kerr Electro-Optic Theory	33
2.1 Kerr Effect in Dielectric Liquids	33
2.1.1 Electric Field Induced Birefringence	33
2.1.2 Linear And Circular Polariscope	34
2.2 Characteristic Parameters	37
2.2.1 Theoretical Derivation from Maxwell Equations	37
2.2.2 Relation Between Kerr Effect and Permittivity Elements	39
2.2.3 Approximate Governing Equations	40
2.2.4 Expressions with Characteristic Parameters	42
2.2.5 Relation between Characteristic Parameters and Electric Field	44
2.3 Onion Peeling Method	44
2.3.1 General Algorithm	45
2.3.2 Two Layer Problem	48

2.3.3	Interpolation from Measured Parameters	51
2.4	Hyperboloid of Revolution Electrode	61
2.4.1	Analytic Solutions for Electric Field	61
2.4.2	Electric Field Approximation for Sharp Point Electrode	64
	Case 1: Near the ground plane ($x \ll d$) and near the centerline ($r \ll d$)	65
	Case 2: At the electrode tip level ($x \approx d$) but not near the tip ($d - x \ll r$)	65
	Case 3: Near the electrode tip ($\eta \ll 1, \theta \ll 1$)	66
	Case 4: Near the ground plane ($\theta \approx \pi/2$) and far away from the center line ($\eta \gg 1$ or $r \gg d$)	66
2.4.3	Closed Forms of Characteristic Parameters	67
	Light Path Through the Centerline $y = 0$	67
	Light Path Along the Surface of Ground Plane $x = 0$	69
2.5	Disturbances from Air Bubbles, Moisture and Other Impurities	70
2.5.1	Disturbance From Insulating Impurities, Such as Air Bubbles	70
2.5.2	Disturbances From Conducting Impurities Such as Moisture	79
2.6	Surface Charge Effects	79
2.7	Unipolar Steady State Space Charge Effect Analysis	87
2.7.1	Parallel Plate Electrodes	88
	Space Charge Limited Conduction	89
	Charge Injected From the Positive Electrode	90
	Charge Injected From the Negative Electrode	91
2.7.2	Coaxial Cylindrical Electrodes	92
	Space Charge Limited Conduction	96
	Positive Charge Injected from Inner Cylinder	98
	Negative Charge Injected from Outer Cylinder	99
2.7.3	Applying Negative Voltage	100
2.7.4	Summary of Space Charge Effects on Electric Field	101
2.7.5	Numerical Analysis of Space Charge Effects on Electric Field and Characteristic Parameters Using Point Plane Electrodes	102
2.8	Summary	108
3	Experimental Apparatus and Software	109
3.1	Optical Components	110
3.1.1	Laser	110
3.1.2	Mirror	111
3.1.3	Polariscope System	113
	Polarizer	113
	Quarter Wave Plate	114
	Kerr Cell	115
	The Whole System	117

3.1.4	Lens	117
3.1.5	Photo-Detector	118
3.2	Instrumentation	118
3.2.1	Vacuum System	118
3.2.2	Circulation System	119
3.2.3	Electronic Instruments	120
	High Voltage Amplifier	120
	Function Generator	122
	Lock-In Amplifier	122
3.2.4	Positioning System	123
	Linear Stepper Motors	123
	Rotational Stepper Motors	123
	Micrometer	124
3.2.5	Calibration of Laser Position	124
3.3	AC High Voltage Modulation	125
3.4	Effects of Applied Voltage Fluctuations	128
3.5	Experimental Procedures	129
3.6	Experimental Errors Due to Polarizer and Quarter Wave Plate	130
	3.6.1 Effects of Nonuniform Polarizer Attenuation	130
	3.6.2 Effects of Imperfect Incident Circularly Polarized Light	130
3.7	Electrical Interfaces	132
	3.7.1 GPIB Interface	132
	3.7.2 Digital Interface	132
3.8	Software	133
	3.8.1 Automation Program	133
	3.8.2 Ansoft Maxwell 2D/3D Electrostatic Simulations	133
3.9	Summary	140
4	Electrode Geometries	141
4.1	Parallel Plate Electrodes	141
4.2	Axisymmetric Geometry	142
	4.2.1 Point-Plane Geometry	142
	4.2.2 Point-Plane-Ring Geometry	146
	Multiple Layer Ring Electrodes	146
	Single-Layer Ring Electrodes	146
4.3	Non-axisymmetric Geometry	165
4.4	Summary	167
5	Demonstration of Onion Peeling Method	169
5.1	Point-Plane Electrodes	170
5.2	Point-Ring-Plane Electrodes	171

5.3	Summary	187
6	Measurements in Transformer Oil	189
6.1	Properties of Transformer Oil	189
6.2	Kerr Constant Measurements with Parallel Plate Electrodes	189
6.3	Measurements with Point-Plane Electrodes	190
6.3.1	Normalization of Characteristic Parameters and Recovered Electric Field	190
6.3.2	Spatial Averaging of the Optical Signal	191
6.3.3	Stainless Steel Point Electrodes	196
	Large Ground Plane	196
	Sensitivity Check	202
	Small Ground Plane	215
6.3.4	With Teflon Film on the Ground Plane: Surface Charge Effects	223
6.4	Measurements with Point-Ring-Plane Electrodes	225
6.4.1	No Dielectric Breakdown Spot on the Ground Plane	225
6.4.2	Numerical Calculation of Characteristic Parameters Near the Sharp Needle tip	228
6.4.3	Dielectric Breakdown Spot on the Ground Plane: Space Charge Effects	228
6.5	Summary	232
7	Measurements in Propylene Carbonate	233
7.1	Propylene Carbonate	233
7.2	Conduction Current Interference and Frequency Dependence	234
7.3	Axisymmetric Measurements	238
7.4	The Difficulties of Doing Experiments in Propylene Carbonate	238
7.5	Sensitivity Check	239
7.6	Non-Axisymmetric Measurements	264
7.7	NMR Spectrum	270
7.8	Summary	279
8	Summary and Conclusions	281
8.1	Summary of Thesis	281
8.2	Accuracy	283
8.3	Suggestions for Future Work	284
8.3.1	Better Algorithm for Electric Field Reconstruction	284
	In Axisymmetric Geometries with High Electric Field Outside Measurement Range	284
	In Non-axisymmetric Geometries	284
8.3.2	Additives in Transformer Oil to Increase Space Charge Effects	284

8.3.3	Surface Charge Effects	285
8.3.4	Better Resolution	285
8.3.5	Larger Windows	285
A	Automation Program	287
B	Electric Field Reconstruction Program: Onion Peeling Method	327
C	Characteristic Parameter Computation	333
D	Beam Averaged Characteristic Parameters	337
	Bibliography	342

Acknowledgments

List of Figures

2.1	The transverse component \mathbf{E}_T of applied electric field in the $x - y$ plane, where φ is the angle between the x axis and \mathbf{E}_T	33
2.2	Optical component arrangement for linear and circular polariscopes.	36
2.3	An n-layer discretization of an axisymmetric electric field region to be used with the onion peeling method.	45
2.4	Relation of electric field components E_x, E_y within the same ring j but different angle θ	47
2.5	A two-layer discretization of an axisymmetric electric field region to be used as a simple case study for the onion peeling method.	50
2.6	Representative measured characteristic parameters using point-plane electrodes under applied AC voltage ≈ 1 kVrms used to recover the electric field using the onion peeling method where $(\gamma_{ac})_N = \gamma_{ac}/V_{AC}^2$ with γ_{ac} and V_{AC} being rms values.	54
2.7	Comparison of electric field components from space charge free theory and reconstructed electric field using the onion peeling method with 20 discretized rings but without smoothing the data in Figure 2.6.	55
2.8	Comparison of electric field components from space charge free theory and reconstructed electric field using the onion peeling method with 160 discretized rings but without smoothing the data in Figure 2.6.	56
2.9	Comparison of electric field components from space charge free theory and reconstructed electric field using the onion peeling method with 20 discretized rings and smoothing the data in Figure 2.6.	57
2.10	Comparison of electric field components from space charge free theory and reconstructed electric field using the onion peeling method with 160 discretized rings and smoothing the data in Figure 2.6.	58
2.11	Comparison of electric field components from space charge free theory and reconstructed electric field using the onion peeling method with 160 ring layers whose outermost ring extended to 10 mm with smoothing of the data.	59

LIST OF FIGURES

2.12	Comparison of electric field components from space charge free theory and reconstructed electric field using the onion peeling method under the semi-infinite line charge assumption to characterize the electric field outside the outermost ring [11].	60
2.13	Prolate spheroidal coordinate [14].	62
2.14	Hyperboloid of revolution electrode.	64
2.15	Comparison of the $h(x) = \frac{2\gamma}{\pi BA^2}$ function defined in eq. (2.145) between analytical solution and numerical calculation with $d = 5$ mm, $R_c = 550\mu\text{m}$, so that $a = \sqrt{d^2 + dR_c} \approx 5.27$ mm.	69
2.16	Local spherical coordinate system with origin at the particle center (x_0, y_0, z_0) in the reference coordinate system (x, y, z) showing the perturbation dipole field $\vec{e} = e_r\hat{r} + e_\theta\hat{\theta}$ due to the induced electric dipole in the particle from the imposed electric field E_0	71
2.17	$\left \frac{\delta\gamma}{\gamma}\right $ is calculated for different heights of light paths 1, 2, 3, 4 passing through the center line $r = 0$ in the presence of a bubble near the electrode tip with center at $x_0 = 4.3$ mm, $y_0 = 0$ as a function of z_0 . Paths 1, 2, 3, 4 are at $x = 4.7$ mm, 3.8 mm, 2.5 mm and 0 and $y = 0$	75
2.18	$\left \frac{\delta\gamma}{\gamma}\right $ is calculated for different heights of light paths 1, 2, 3, 4 passing through the center line $r = 0$ in the presence of a bubble near the ground plane with center at $x_0 = 0.5$ mm, $y_0 = 0$ as a function of z_0 . Paths 1, 2, 3, 4 are at $x = 4.7$ mm, 3.8 mm, 2.5 mm and 0 and $y = 0$	76
2.19	$\left \frac{\delta\gamma}{\gamma}\right $ for light paths at $x = 4.7$ mm but different y coordinates with different bubble positions 1, 2, 3, 4, respectively. In these Figures, bubble center position 1 is at (4.3, 0.7, 0) mm, bubble center position 2 is at (4.3, 2.5, 0) mm, bubble center position 3 is at (4.3, 10, 0) and bubble center position 4 is at (4.3, 50, 0) mm. The horizontal axis is the light path y coordinate.	77
2.20	$\delta\alpha$ for the light paths at $x = 4.7$ mm but different y coordinates with different bubble positions 1, 2, 3, 4, respectively. Bubble center position 1 is at (4.3, 0.7, 0) mm, bubble center position 2 is at (4.3, 2.5, 0) mm, bubble center position 3 is at (4.3, 10, 0) and bubble center position 4 is at (4.3, 50, 0) mm. The horizontal axis is the light path y coordinate.	78
2.21	Hyperboloid of revolution approximation for point-plane electrodes with a Teflon film on the ground plane.	80
2.22	The equipotential lines for a point-plane electrode geometry with a thin Teflon film ($\sigma_2 \approx 0$) on the surface of the ground plane. We see that except around the center, most of the equipotential lines are normal to the film surface, which means that the electric field just above the surface of the Teflon film is tangential.	82

2.23 The calculated electric field component E_r for point-plane electrodes with $R_c = 550\mu\text{m}$ and $d = 5$ mm, with and without a thin Teflon film on the ground plane with a transformer oil dielectric as a function of r for $x = 2.54, 3.81, 4.78$ mm under an applied DC voltage 1 V. . . . 84

2.24 The calculated electric field component E_x for point-plane electrodes with $R_c = 550\mu\text{m}$ and $d = 5$ mm, with and without a thin Teflon film on the ground plane with a transformer oil dielectric as a function of r for $x = 2.54, 3.81, 4.78$ mm under an applied DC voltage 1 V. . . . 85

2.25 The calculated electric field component E_x with and without a thin Teflon film on the ground plane with a transformer oil dielectric at $x = 0.25$ mm as a function of r with an applied DC voltage 1 V. . . . 86

2.26 Parallel plate electrodes where either positive volume charge is injected from the positive electrode or negative volume charge is injected from the negative electrode. 88

2.27 Steady state electric field distributions for various current values in the presence of positive space charge between parallel plate electrodes, injected from the positive electrode at $x = 0$. In this figure, the area under each curve is equal to $V_0 = 10000$ volts. 91

2.28 Steady state positive space charge distributions for various current values between parallel plate electrodes for positive charge injected from the positive electrode at $x = 0$ 92

2.29 Steady state electric field distributions for various current values in the presence of negative space charge between parallel plate electrodes, injected from the negative electrode at $x = h = 0.1$ m. Note that the area under each curve is equal to $V_0 = 10000$ volts. 93

2.30 Steady state negative space charge distributions for various current values between parallel plate electrodes for negative charge injected from the negative electrode at $x = h = 0.1$ m. 94

2.31 Coaxial cylinder conductors 95

2.32 Steady state electric field distributions for various current values in the presence of positive space charge injected from the positive inner cylinder at $r = a = 0.05$ m. 98

2.33 Steady state positive space charge distributions for positive charge injection from the inner cylinder at $r = a = 0.05$ m. 99

2.34 Steady state electric field distributions for various current values in the presence of negative space charge injected from the outer cylinder at $r = b = 0.1$ m. 100

2.35 Steady state negative space charge distributions for negative charge injection from the outer cylinder at $r = b = 0.1$ m. 101

2.36 A circular column of space charge with 2 mm radius and charge density of 0.00001 C/m³ between point-plane electrodes with point radius of curvature $R_c = 550\mu\text{m}$ and gap distance $d = 5$ mm. 103

LIST OF FIGURES

2.37	Calculated electric field component E_r for different values of x as a function of r , comparing the cases with (thick lines) and without (thin lines) the space charge distribution of Figure 2.36 under applied DC voltage of 10 kV.	104
2.38	Calculated electric field component E_x for different values of x as a function of r , comparing the cases with (thick lines) and without (thin lines) the space charge distribution of Figure 2.36 under applied DC voltage of 10 kV.	105
2.39	Calculated optical characteristic parameter α for different values of x as a function of y , comparing the cases with (thick lines) and without (thin lines) the space charge distribution of Figure 2.36 with an applied DC voltage of 10 kV.	106
2.40	Calculated normalized characteristic parameter γ_N for different values of x as a function of y , comparing the cases with (thick lines) and without (thin lines) the space charge distribution of Figure 2.36 with an applied DC voltage of 10 kV.	107
3.1	Picture of experimental apparatus.	110
3.2	Top and side view of the experimental apparatus arrangement for incident light intensity I_i just after the filtering polarizer and output light intensity I_o after the analyzing polarizer.	112
3.3	Interconnection of electronic instruments.	120
3.4	When we simultaneously apply AC and DC high voltages to the Kerr cell electrodes, there will be AC and DC electric fields that are not collinear if space charge is present.	125
3.5	Window of Maxwell 3D Simulator for a non-axisymmetric point-plane electrode geometry.	135
3.6	Model drawing environment in Maxwell 3D Simulator for the electrode geometry of Figure 3.5.	136
3.7	Window to set up materials properties.	137
3.8	Window to set up boundary conditions and source values.	138
3.9	Window of post processor of the electrode geometry in Figure 3.5.	139
4.1	Point-plane electrode geometry with large ground plane.	143
4.2	Stainless steel needle electrode with radius of curvature $\approx 550\mu\text{m}$ and length ≈ 7 cm.	144
4.3	Aluminum needle electrode with radius of curvature $\approx 1050\mu\text{m}$ and length ≈ 7 cm.	145
4.4	High voltage point-ring electrode with multiple layer rings. The center point electrode is 2.5 mm above the ground plane and the surrounding ring electrodes are 5 mm above the ground plane.	148

4.5 The simulated electric field component E_r for different x values as a function of r using multiple layer (3 layers) point-ring-plane electrodes whose high voltage electrodes are shown in Figure 4.4 under applied DC voltage 1 kV. 149

4.6 The simulated electric field component E_x for different x values as a function of r using multiple layer (3 layers) point-ring-plane electrodes whose high voltage electrodes are shown in Figure 4.4 under applied DC voltage 1 kV. 150

4.7 The calculated optical characteristic parameter α from calculated electric field components shown in Figures 4.5 and 4.6 for different x values as a function of y from $y = 0$ to $y = 100$ mm using multiple layer (3 layers) point-ring-plane electrodes whose high voltage electrode is shown in Figure 4.4. 151

4.8 The calculated normalized optical characteristic parameter γ_N (defined in Section 6.3.1) from simulated electric field components shown in Figures 4.5 and 4.6 for different x values as a function of y from $y = 0$ to $y = 100$ mm using multiple layer (3 layers) point-ring-plane electrodes whose high voltage electrode is shown in Figure 4.4. 152

4.9 The calculated optical characteristic parameter α from calculated electric field components shown in Figures 4.5 and 4.6 for different x values as a function of y from $y = 0$ to $y = 10$ mm using multiple layer (3 layers) point-ring-plane electrodes whose high voltage electrode is shown in Figure 4.4. 153

4.10 The calculated normalized optical characteristic parameter γ_N (defined in Section 6.3.1) from simulated electric field components shown in Figures 4.5 and 4.6 for different x values as a function of y from $y = 0$ to $y = 10$ mm using multiple layer (3 layers) point-ring-plane electrodes whose high voltage electrode is shown in Figure 4.4. 154

4.11 High voltage point-ring electrode with a single layer ring. 155

4.12 Aluminum needle electrode used in the point-ring-plane electrodes as the center sharp point electrode with radius of curvature $\approx 40\mu\text{m}$ and length ≈ 7 cm. 156

4.13 Point-ring-plane electrode structure showing the point electrode being ~ 2.5 mm below the ring electrode. 157

4.14 Space charge free equipotential lines for point-ring-plane electrode on the cross section of $x - y$ plane under applied DC voltage 1000 volts. 158

4.15 The calculated electric field component E_r for different x values as a function of r using the single layer point-ring-plane electrodes whose high voltage electrode is shown in Figures 4.11 and 4.13 under applied DC voltage 1 kV. 159

LIST OF FIGURES

4.16	The calculated electric field component E_x for different x values as a function of r using the single layer point-ring-plane electrodes whose high voltage electrode is shown in Figures 4.11 and 4.13 under applied DC voltage 1 kV.	160
4.17	The calculated optical characteristic parameter α from calculated electric field components shown in Figures 4.5 and 4.6 for different x values as a function of y from $y = 0$ to $y = 100$ mm using single layer point-ring-plane electrodes whose high voltage electrodes are shown in Figures 4.11 and 4.13.	161
4.18	The calculated normalized optical characteristic parameter γ_N (defined in Section 6.3.1) from calculated electric field components shown in Figures 4.5 and 4.6 for different x values as a function of y from $y = 0$ to $y = 100$ mm using single layer point-ring-plane electrodes whose high voltage electrode is shown in Figures 4.11 and 4.13.	162
4.19	The calculated optical characteristic parameter α from calculated electric field components shown in Figures 4.5 and 4.6 for different x values as a function of y from $y = 0$ to $y = 10$ mm using single layer point-ring-plane electrodes whose high voltage electrode is shown in Figures 4.11 and 4.13.	163
4.20	The calculated normalized optical characteristic parameter γ_N (defined in Section 6.3.1) from simulated electric field components shown in Figures 4.5 and 4.6 for different x values as a function of y from $y = 0$ to $y = 10$ mm using single layer point-ring-plane electrodes whose high voltage electrode is shown in Figures 4.11 and 4.13.	164
4.21	Non-axisymmetric electrode geometry.	165
4.22	Relative position and dimensions of metal wall and block used in the non-axisymmetric geometry of Figure 4.21.	166
4.23	Relative position of non-axisymmetric metal wall and block to the point electrode as shown in Figure 4.21.	167
5.1	Calculated electric field (rms) components E_r and E_x using the point-plane electrode of Figure 4.2 for $x = 2.54$ mm, $x = 3.81$ mm and $x = 4.78$ mm below the tip of the point electrode as a function of r under space charge free conditions with voltage 1 kVrms.	173
5.2	Electric field (rms) comparison between simulation results (solid lines) from Maxwell Simulator and reconstruction algorithm (dashed lines) using the onion peeling method from calculated characteristic parameters in Figures 2.39 and 2.40 under an applied AC voltage 1 kVrms.	174
5.3	Calculated electric field (rms) components E_r and E_x using the point-plane electrode of Figure 4.2 for $x = 6.35$ mm and $x = 10.5$ above the tip of the point electrode as a function of r under space charge free conditions at AC voltage 1 kVrms.	175